

Weakly nonlinear Rayleigh-Taylor instability of finite-thickness fluid supported by a semi-infinite fluid

Hong-Yu Guo(郭宏宇), Dong-Yu Guo(郭懂宇), Ben-Jin Guan(关本金), Ying-Jun Li(李英骏), and Shi-Qi Liu(刘世奇)
Citation: Chin. Phys. B, 2026, 35 (**6**): 065202. DOI: 10.1088/1674-1056/ae1de9
http://cpb.iphy.ac.cn; http://iopscience.iop.org/cpb

What follows is a list of articles you may be interested in

Dependence of Rayleigh-Taylor instability of finite-thickness shell on initial perturbed wavelengths

Hong-Yu Guo(郭宏宇), Ben-Jin Guan(关本金), Li-Feng Wang(王立锋), Zhi-Yuan Li(李志远), and Ying-Jun Li(李英骏)
Chin. Phys. B, 2025, 34 (**11**): 115202. DOI: 10.1088/1674-1056/ade06b

Scaling of rise time of drive current on development of magneto-Rayleigh-Taylor instabilities for single-shell Z-pinches

Xiaoguang Wang(王小光), Guanqiong Wang(王冠琼), Shunkai Sun(孙顺凯), Delong Xiao(肖德龙), Ning Ding(丁宁), Chongyang Mao(毛重阳), and Xiaojian Shu(束小建)
Chin. Phys. B, 2022, 31 (**2**): 025203. DOI: 10.1088/1674-1056/ac1fd9

Weakly nonlinear multi-mode Bell–Plesset growth in cylindrical geometry

Hong-Yu Guo(郭宏宇), Tao Cheng(程涛), and Ying-Jun Li(李英骏)
Chin. Phys. B, 2020, 29 (**11**): 115202. DOI: 10.1088/1674-1056/ab9c14

Coupling between velocity and interface perturbations in cylindrical Rayleigh-Taylor instability

Hong-Yu Guo(郭宏宇), Li-Feng Wang(王立锋), Wen-Hua Ye(叶文华), Jun-Feng Wu(吴俊峰), Wei-Yan Zhang(张维岩)
Chin. Phys. B, 2018, 27 (**5**): 055205. DOI: 10.1088/1674-1056/27/5/055205

Rayleigh-Taylor instability at spherical interfaces of incompressible fluids

Hong-Yu Guo(郭宏宇), Li-Feng Wang(王立锋), Wen-Hua Ye(叶文华), Jun-Feng Wu(吴俊峰), Ying-Jun Li(李英骏), Wei-Yan Zhang(张维岩)
Chin. Phys. B, 2018, 27 (**2**): 025206. DOI: 10.1088/1674-1056/27/2/025206

Weakly nonlinear Rayleigh–Taylor instability of finite-thickness fluid supported by a semi-infinite fluid

Hong-Yu Guo(郭宏宇)[1,2,3,†], Dong-Yu Guo(郭懂宇)[1,2,†,‡], Ben-Jin Guan(关本金)[4], Ying-Jun Li(李英骏)[4], and Shi-Qi Liu(刘世奇)[1,2,§]

[1] *School of Energy and Mining Engineering, China University of Mining and Technology-Beijing, Beijing* 100083, *China*
[2] *Mining Water Control and Utilization Engineering Center, Beijing* 100083, *China*
[3] *School of Physics, Beijing Institute of Technology, Beijing* 100081, *China*
[4] *State Key Laboratory for Tunnel Engineering, China University of Mining and Technology, Beijing* 100083, *China*

(Received 5 August 2025; revised manuscript received 26 October 2025; accepted manuscript online 11 November 2025)

Rayleigh–Taylor instability (RTI) in multi-interface shells significantly influences shell deformation and material mixing, thereby affecting inertial confinement fusion (ICF) implosion performance. This study investigates the weakly nonlinear (WN) RTI in a finite-thickness fluid shell supported by a semi-infinite fluid. We derive the governing equations and third-order WN solutions for RTI growth at both interfaces of the shell. Numerical simulations based on the two-dimensional Eulerian framework confirm the validity of the theoretical results in the WN regime. The perturbation growth rate at the lower interface and the interfacial coupling coefficients both exhibit explicit dependence on the Atwood number A and the normalized shell thickness ξ. The WN growth and the deformation of the shell are investigated through the third-order solutions. Comparisons are made with the classical RTI in the WN regime under different initial conditions. Additionally, we analyze the saturation amplitude of the perturbation fundamental mode. It is found that the Atwood number and finite-thickness effects play a pivotal role in the WN evolution of the fluid layer.

Keywords: Rayleigh–Taylor instability, inertial confinement fusion, mode-coupling

PACS: 52.57.Fg, 47.20.Ma, 52.35.Py

DOI: 10.1088/1674-1056/ae1de9 **CSTR:** 32038.14.CPB.ae1de9

1. Introduction

The Rayleigh–Taylor instability[1,2] (RTI) is a fundamental hydrodynamic instability that arises when a denser fluid is accelerated by a lighter one, leading to the exponential growth of interfacial perturbations. RTI is recognized as a dominant mechanism governing the dynamics of high-energy-density systems, with profound implications for astrophysical phenomena such as supernova explosions[3] and energy applications like inertial confinement fusion (ICF).[4,5] Understanding and controlling the growth of RTI is crucial for achieving high-gain implosion experiments, as these milestones bring us closer to realizing clean energy applications through ICF.[6] In ICF central ignition implosion experiments, a fuel capsule typically consists of multiple layers, including at least an outer ablator and an inner fuel shell. This configuration generates at least three interfaces during implosion, namely, the ablation front, the fuel–ablator boundary, and the hot-spot interface. During the acceleration phase of the implosion, the fuel–ablator interface experiences RTI growth, driven by the high-pressure plasma generated from laser-driven ablation. During the subsequent deceleration phase, the hot-spot region becomes susceptible to RTI as the high-density fuel shell decelerates under the influence of the low-pressure ablation plasma. The consequent interfacial instabilities can cause significant mixing of ablation products into the hot spot, degrading fuel compression efficiency and reducing fusion yield. Given its fundamental significance to both basic research and engineering applications in ICF implosions, investigating the growth of RTI during ICF implosion processes remains a critical research focus.[7–9]

The classical Rayleigh–Taylor instability (CRTI) for inviscid, immiscible fluids was first analyzed by Rayleigh[1] and Taylor,[2] who derived the analytical solution for the exponential growth of perturbations at the interface between two semi-infinite fluids. This foundational work established that interface perturbations grow as $\eta(t) \sim \eta_0 \cdot \mathrm{e}^{\gamma t}$, where $\gamma = \sqrt{Akg}$ represents the linear growth rate, with A being the Atwood number, k the wavenumber, and g the gravitational acceleration. RTI plays a critical role in ICF, making it a subject of extensive research over the past decades. Most studies have focused on the classical RTI model, which considers two semi-infinite fluids separated by a single interface while considering various influencing factors.[10–15] Notably, ablation effects have been shown to suppress RTI, al-

[†]These authors contributed equally to this work.
[‡]Corresponding author. E-mail: pzg8559@163.com
[§]Corresponding author. E-mail: 201845@cumtb.edu.cn

© 2026 Chinese Physical Society and IOP Publishing Ltd. All rights, including for text and data mining, AI training, and similar technologies, are reserved.

tering its perturbation growth; rather than increasing exponentially in the classical manner, the growth rate transitions to an ablation-stabilized regime.[12–15] However, interfaces of finite-thickness shell layers can influence and couple with each other through a mechanism called the feedthrough effect. Even when an interface is initially perfectly smooth, perturbations can still emerge via feedthrough from adjacent interfaces. Understanding the coupling mechanisms between perturbations across different interfaces is essential for ICF implosion experiments. Mikaelian[16–18] investigated the linear growth of RTI in systems with an arbitrary number of stratified fluids. The interface coupling mechanisms and linear growth characteristics in three-fluid systems with two material interfaces are discussed through an analytical method. Subsequently, we extended the model to analyze the linear growth of RTI in planar,[19] cylindrical,[20] and spherical[21] geometries, thereby systematically characterizing the interfacial coupling effects in each case. Li[22] employed a second-order Godunov hydrodynamic simulation code to study the initial-phase effects of long-wavelength RTI on thin-shell structures. It was found that large phase differences significantly accelerate instability growth. Recently, the effect of finite resistivity on the magneto-Rayleigh–Taylor instability (MRTI) was discussed by Xiao.[23] The dispersion relation of MRTI is derived through a three-region slab model. All the studies mentioned above are devoted to investigating the RTI growth in the linear regime. During this linear phase, the perturbation amplitude $\eta(t)$ remains significantly smaller than the wavelength λ, which is consistent with the experimental results.[24,25] When the perturbation amplitude $\eta(t)$ attains magnitudes comparable to the perturbation wavelength ($k\eta(t) \sim 1$), the system transitions into the weakly nonlinear (WN) regime. The initially symmetric interface will develop into asymmetric bubble-spike structures. Indeed, in both low-adiabat and high-adiabat ICF implosions,[26,27] perturbation amplitudes can reach levels where linear growth theory ceases to be valid. A comprehensive understanding of RTI growth within the WN regime is essential for accurately predicting perturbation evolution. Notably, the WN model not only reveals the mode-coupling process but also quantitatively captures the physical mechanisms governing transitions from linear to nonlinear instability growth. The WN evolution of the RTI in a finite-thickness (vacuum–fluid–vacuum) shell has been analyzed analytically.[28–30] The coupling coefficient between the two vacuum–fluid interfaces was given by e^{-kd}, where d is the shell thickness. The deformation of the thin shell is effectively captured by this model. When a high-power laser beam irradiates the outer surface of the target, the surface layer generates a low-density plasma layer under such irradiation. During the period from the onset of laser driving to the early stages of shell acceleration, the plasma density remains extremely low and can be approximated as a vacuum region.[31] For simplicity, we focus on RTI involving a double interface, aiming to conduct a principle-level exploration of the interface coupling effect. However, in practical ICF implosions, multiple interfaces are present. Future work will explore the feasibility of adjusting the Atwood number at adjacent interfaces to suppress the growth of perturbations. It is noteworthy that the potential effects of compressibility are not included in this study. When compressibility is taken into account, the additional degrees of freedom introduced by sound waves and compressibility are likely to become significant. The investigation of compressibility effects will be addressed in our future work. From an instability analysis perspective, the key advancement beyond the classical single-interface configuration is the interfacial coupling or feedthrough effects. The minimal two-interface configuration, which incorporates the effects of Atwood numbers (density ratios) at the interfaces, can be used to demonstrate these effects. In this paper, we investigate RTI growth in a finite-thickness shell supported by a semi-infinite fluid during the WN stage.

This paper is organized as follows. Section 2 establishes the theoretical model and develops the third-order analytical solutions for RTI growth. Section 3 displays the WN evolution of RTI under varying initial conditions and interface deformation. The numerical results are also presented. Section 4 summarizes the major results and draws some conclusions.

2. Theoretical model and mathematical formulation

As illustrated in Fig. 1, two incompressible, irrotational, inviscid, and immiscible fluids are immersed in a gravitational field $-g\hat{e}_y$. The lower fluid layer has an infinite extent with density ρ^l, while the upper fluid layer has a thickness d and density ρ^u. A two-dimensional Cartesian coordinate system is established, where x and y represent the directions along and normal to the lower interface of the fluid shell, respectively. The initial unperturbed lower and upper interfaces are located at $y = 0$ (separating ρ^l and ρ^u) and $y = d$ (free surface), respectively. In the following analyses, physical quantities associated with the upper fluid layer will be denoted by the superscript "u", while those corresponding to the lower fluid layer will be marked with the superscript "l", unless explicitly stated otherwise. The velocity potential theory provides a rigorous mathematical framework for characterizing an incompressible fluid layer. The velocity potential can be decomposed into unperturbed and perturbed components as

$$\Phi^i(x,y,t) = \Phi^i_{(0)}(t) + \phi^i(x,y,t), \tag{1}$$

where $\Phi^i_{(0)}(t)$ denotes the unperturbed velocity potential and $\phi^i(x,y,t)$ the perturbation ($i = u, l$), respectively. The dynamic

pressure conditions at both interfaces are described by the Bernoulli equation, which can be expressed as

$$p^i = -\rho^i\left[\Phi_t^i + \frac{1}{2}(\nabla\Phi^i)^2 + gy + f(t)\right]. \tag{2}$$

The interfacial pressure can be similarly decomposed into equilibrium and perturbed components as $p^i = p^i_{(0)} + \tilde{p}^i$, with $p^i_{(0)}$ representing the equilibrium pressure and $\tilde{p}^i$ denoting the perturbed pressure. As can be seen, the equilibrium pressure condition $p^l_{(0)} - p^u_{(0)} = \rho^u g d$ has been satisfied for the unperturbed pressures. The boundary conditions at the upper interface are governed by

$$\eta^u_t + \phi^u_x\cdot\eta^u_x - \phi^u_y = 0 \quad \text{at} \quad y = d+\eta^u, \tag{3}$$

$$\tilde{p}^u = \rho^u\left[\phi^u_t + \frac{1}{2}(\nabla\phi^u)^2 + g\eta^u\right] = 0 \quad \text{at} \quad y = d+\eta^u, \tag{4}$$

where Eq. (3) means the normal components of velocity should be equal to the normal component of the fluid velocity and Eq. (4) denotes that the perturbed pressure at the free surface is zero for a finite-thickness fluid layer,[28,29] namely, $\tilde{p}^u = 0$. The governing equations at the lower interface are expressed as

$$\eta^l_t + \phi^u_x\cdot\eta^l_x - \phi^u_y = 0 \quad \text{at} \quad y = \eta^l, \tag{5}$$

$$\eta^l_t + \phi^l_x\cdot\eta^l_x - \phi^l_y = 0 \quad \text{at} \quad y = \eta^l, \tag{6}$$

$$\rho^u\left[\phi^u_t + \frac{1}{2}(\nabla\phi^u)^2 + g\eta^u + f(t)\right] = \rho^l\left[\phi^l_t + \frac{1}{2}(\nabla\phi^l)^2 + g\eta^l + f(t)\right] \quad \text{at} \quad y = \eta^l. \tag{7}$$

Equations (5) and (6) represent the kinematic boundary condition, i.e., the normal component of the velocity near the interface is continuous. Equation (7) means the pressure continuous condition across the lower interface. Thus, the governing equations for the system are Eqs. (3)–(7).

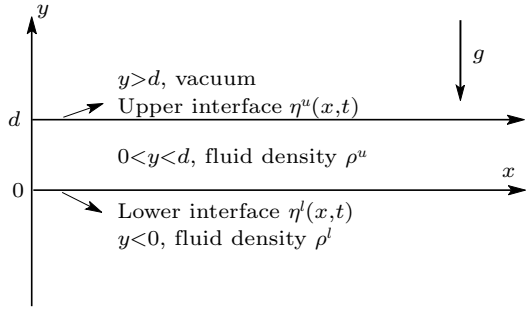


Fig. 1. Schematic illustration of the fluid layer employed in this study.

The perturbations and perturbed velocity potentials are expanded as an p-th order power series in the formal small parameter ϵ:

$$\eta^u(x,t) = \sum_{n=1}^{p}\epsilon^{n+2m}\sum_{m=0}^{q}\eta^u_{n+2m,n}(t)\cos(nkx), \tag{8}$$

$$\eta^l(x,t) = \sum_{n=1}^{p}\epsilon^{n+2m}\sum_{m=0}^{q}\eta^l_{n+2m,n}(t)\cos(nkx), \tag{9}$$

$$\phi^u(x,y,t) = \sum_{n=1}^{p}\epsilon^{n+2m}\sum_{m=0}^{q}\left[A_{n+2m,n}(t)\,\mathrm{e}^{nky} + B_{n+2m,n}(t)\,\mathrm{e}^{-nky}\right]\cos(nkx), \tag{10}$$

$$\phi^l(x,y,t) = \sum_{n=1}^{p}\epsilon^{n+2m}\sum_{m=0}^{q}C_{n+2m,n}(t)\,\mathrm{e}^{nky}\cos(nkx), \tag{11}$$

where $\eta^i_{n+2m,n}(t)\cos(nkx)$ represents the nth-order component of the interface deformation at the upper and lower interfaces. Here, $q = \lfloor\frac{p-n}{2}\rfloor$, where the Gauss symbol $\lfloor\cdot\rfloor$ indicates the largest integer less than or equal to $\frac{p-n}{2}$. The terms with $m=0$ correspond to the nth harmonic generation, while those with $m>0$ represent the $(n+2m)$th-order feedback. For instance, when considering terms up to the third order ($p=3$), the position of the lower interface can be expressed as

$$\eta^l(x,t) = \epsilon^1\eta^l_{1,1}(t)\cos(kx) + \epsilon^2\eta^l_{2,2}(t)\cos(2kx) + \epsilon^3\left[\eta^l_{3,3}(t)\cos(3kx) + \eta^l_{3,1}(t)\cos(kx)\right]. \tag{12}$$

Noting that the velocity potential $\phi^i(x,y,t)$ has satisfied the Laplace equation $\nabla^2\phi^i = 0$ and the boundary condition $\nabla\phi^l|_{y\to-\infty} = 0$, we substitute Eqs. (8)–(11) into the governing Eqs. (3)–(7). Then, we perform Taylor expansions about the unperturbed interfaces $y=0$ and $y=d$. By systematically collecting terms of identical order of the parameter ϵ^n, we establish a series of coupled equations. Once these equations are obtained, the formal parameter ϵ is subsequently set to unity ($\epsilon = 1$) to obtain the physical solutions. This enables us to solve these equations step-by-step.

At the first-order $O(\epsilon)$, the governing equations for $\eta^u_{1,1}$ and $\eta^l_{1,1}$ are

$$\ddot{\eta}^u_{1,1} - \frac{2\,\mathrm{e}^{-\xi}}{1+\mathrm{e}^{-2\xi}}\ddot{\eta}^l_{1,1} + \frac{1-\mathrm{e}^{-2\xi}}{1+\mathrm{e}^{-2\xi}}\eta^u_{1,1} = 0, \tag{13}$$

$$\ddot{\eta}^l_{1,1} - \frac{\mathrm{e}^{-\xi}(1+A)}{1+A\,\mathrm{e}^{-2\xi}}\ddot{\eta}^u_{1,1} - A\frac{1-\mathrm{e}^{-2\xi}}{1+A\,\mathrm{e}^{-2\xi}}\eta^l_{1,1} = 0, \tag{14}$$

where $A = \left(\rho^u-\rho^l\right)/\left(\rho^u+\rho^l\right)$ is the Atwood number and $\xi = kd$ represents the normalized upper shell thickness. The notation $\ddot{\eta}^i_{1,1} = d^2\eta^i_{1,1}/\mathrm{d}\tau^2$ indicates the second derivative with respect to the normalized time $\tau = \sqrt{kg}t$. Considering the most common initial conditions where the fluid layer is initially at rest with identical wavelength perturbations on both interfaces, specified by

$$\eta^u_{1,1}(0) = u_0, \quad \eta^l_{1,1}(0) = l_0, \quad \dot{\eta}^u_{1,1}(0) = 0, \quad \dot{\eta}^l_{1,1}(0) = 0. \tag{15}$$

Thus, the linear growth of interface perturbation can be obtained as

$$\eta^u_{1,1} = \frac{1}{1-\alpha_+\alpha_-}\left[(u_0-\alpha_+ l_0)\cos\tau + \alpha_+(l_0-\alpha_- u_0)\cosh\Gamma\right], \tag{16}$$

$$\eta^l_{1,1} = \frac{1}{1-\alpha_+\alpha_-}\big[(l_0-\alpha_- u_0)\cosh\Gamma + \alpha_-(u_0-\alpha_+ l_0)\cos\tau\big], \tag{17}$$

where the coupling coefficients $\alpha_- = \mathrm{e}^{-\xi}$ and $\alpha_+ = 2A\,\mathrm{e}^{-\xi}/(1+A)$ represent interfacial feedback mechanisms between the upper and lower boundaries. The linear solution demonstrates distinct growth characteristics of perturbations across different interfaces. The upper interface demonstrates harmonic oscillation with characteristic frequency $\omega = \sqrt{kg}$. The lower interface exhibits exponential growth described by $\Gamma = \gamma t$, where the growth rate γ is derived as

$$\gamma = \sqrt{Akg\frac{1-\mathrm{e}^{-2\xi}}{1-A\,\mathrm{e}^{-2\xi}}}. \tag{18}$$

As can be seen, the growth rate shows explicit dependence on the shell thickness d (through ξ) and the Atwood number A. When $A = 1$, the growth rate $\gamma_c = \sqrt{kg}$ for Taylor's result is recovered. For a finite density of the lower fluid ($A \neq 1$) in the thick shell limit $\xi \gg 1$, the linear growth rate reduces to $\gamma = \sqrt{Akg}$ for CRTI.[10] This asymptotic limit corresponds precisely to the growth behavior observed in systems with two semi-infinite fluids. In the thin shell limit, the growth rate takes the form

$$\gamma(\xi \ll 1) \approx k\sqrt{\frac{2Agd}{1-A}}. \tag{19}$$

As can be seen, under the thin-shell approximation, the growth rate scales linearly with the wavenumber k, whereas in classical RTI, the growth rate scales with $\sqrt{k}$.

The interfacial coupling phenomenon is explicitly manifested in the linear solutions, where $\eta^u_{1,1}$ and $\eta^l_{1,1}$ are fully determined by the initial perturbations u_0 and l_0. The upper interface is initially stable and exhibits oscillatory behavior which is characterized by the $\cos\tau$ term. The lower interface is subject to RTI, with perturbations growing exponentially as characterized by the $\cosh\Gamma$ term. When considering finite-thickness shells, the coupling effect between interfaces becomes significantly enhanced, particularly when $\xi < 1$. The downward feedthrough from the upper to the lower interface is governed by the factor α_-, which depends solely on the shell thickness ξ. The upward coupling from the lower to the upper interface is characterized by the factor α_+, which explicitly depends on both the Atwood number A and the shell thickness ξ. For $A = 1$, the linear solution for RTI growth in a finite-thickness shell is recovered.[28]

The linear solutions presented in Eqs. (16) and (17) contain an exponentially growing mode ($\cosh\Gamma$) and an oscillatory mode ($\cos\tau$). Notably, when the initial condition $l_0 = \mathrm{e}^{-\xi}u_0$ is satisfied, the growing modes at both interfaces are completely suppressed, rendering the system stable except for initial oscillations. When the condition $u_0 = \alpha_+ l_0$ is imposed, the oscillatory modes are entirely eliminated. Furthermore, the analysis demonstrates that canceling either mode at one interface automatically cancels the corresponding mode at the other interface. In the limit of large shell thickness ($\xi \to \infty$), the interface coupling becomes negligible, reducing the system to two decoupled interfaces. Under this condition, the solutions simplify to

$$\eta^u_{1,1} = u_0\cos(\sqrt{kg}t), \tag{20}$$

$$\eta^l_{1,1} = l_0\cosh(\sqrt{Akg}t), \tag{21}$$

which represents the solutions for CRTI at the upper and lower interfaces of an infinitely thick fluid, respectively.

For the second-order $O(\epsilon^2)$, the governing equations for $\eta^u_{2,2}$ and $\eta^l_{2,2}$ are

$$\begin{aligned}
&\ddot\eta^u_{2,2} - \frac{2\,\mathrm{e}^{-2\xi}}{1+\mathrm{e}^{-4\xi}}\ddot\eta^l_{2,2} + 2\frac{1-\mathrm{e}^{-4\xi}}{1+\mathrm{e}^{-4\xi}}\eta^u_{2,2}\\
&-f_1\Big[\eta^l_{1,1}\ddot\eta^l_{1,1} + \eta^u_{1,1}\ddot\eta^u_{1,1} + 2\dot\eta^l_{1,1}\dot\eta^l_{1,1}\\
&-\mathrm{sech}\xi\ \eta^l_{1,1}\ddot\eta^u_{1,1} - 4\cosh\xi\ \dot\eta^l_{1,1}\dot\eta^u_{1,1}\\
&-\mathrm{sech}\xi\cdot\cosh(2\xi)\eta^u_{1,1}\ddot\eta^l_{1,1} + 2\cosh^2\xi\ \dot\eta^u_{1,1}\dot\eta^u_{1,1}\Big],
\end{aligned} \tag{22}$$

$$\begin{aligned}
&\ddot\eta^l_{2,2} - \frac{(1+A)\,\mathrm{e}^{-2\xi}}{1+A\,\mathrm{e}^{-4\xi}}\ddot\eta^u_{2,2} - 2A\frac{1-\mathrm{e}^{-4\xi}}{1+A\,\mathrm{e}^{-4\xi}}\eta^l_{2,2}\\
&+f_2\big[\eta^l_{1,1}\ddot\eta^l_{1,1} + \eta^u_{1,1}\ddot\eta^u_{1,1} + 2\dot\eta^u_{1,1}\dot\eta^u_{1,1}\\
&-\mathrm{sech}\xi\ \eta^u_{1,1}\ddot\eta^l_{1,1} - 4\cosh\xi\ \dot\eta^l_{1,1}\dot\eta^u_{1,1}\\
&-\mathrm{sech}\xi\cdot\cosh(2\xi)\ \eta^l_{1,1}\ddot\eta^u_{1,1}\\
&+2\left(1+\alpha_+\sinh^2\xi/\alpha_-\right)\dot\eta^l_{1,1}\dot\eta^l_{1,1}\big],
\end{aligned} \tag{23}$$

the coefficients f_1 and f_2 are

$$f_1 = \coth\xi\ \mathrm{sech}(2\xi), \tag{24}$$

$$f_2 = \mathrm{e}^{-2\xi}\coth\xi\ (1+A)/\left(1+A\,\mathrm{e}^{-4\xi}\right). \tag{25}$$

The coupled second-order ordinary differential equations for $\eta^u_{2,2}$ and $\eta^l_{2,2}$ display explicit dependence on both the Atwood number A and the shell thickness ξ. This coupling makes obtaining exact analytical solutions particularly challenging. To derive higher-order WN solutions, we implement the following approximation: all oscillatory terms (those containing $\cos\tau$, $\cos^2\tau$, $\cos^3\tau$) are neglected, while retaining only the dominant growth terms (those with $\cosh\Gamma$, $\cosh^2\Gamma$, $\cosh^3\Gamma$) at each order. Consequently, the linear solutions reduce to

$$\eta^u_{1,1} = \alpha_+\Xi\cosh\Gamma, \tag{26}$$

$$\eta^l_{1,1} = \Xi\cosh\Gamma, \tag{27}$$

where the amplitude Ξ is defined as $\Xi = \frac{(l_0-\mathrm{e}^{-\xi}u_0)}{(1-\alpha_+\alpha_-)}$.

Then, the solutions for $\eta^u_{2,2}$ and $\eta^l_{2,2}$ can be obtained by solving Eqs. (22) and (23) as

$$\eta^u_{2,2} = -\frac{k}{2}a_0\alpha_+\Xi^2\,\mathrm{e}^{-\xi}(a_1A^3 + a_2A^2$$

$$+a_3A+9\mathrm{e}^{-2\xi}-3)\cosh^2\Gamma, \tag{28}$$

$$\eta^l_{2,2} = -\frac{k}{2}a_0\Xi^2(a_4A^3+a_5A^2+a_6A+3\mathrm{e}^{-2\xi} +3\mathrm{e}^{-4\xi})\cosh^2\Gamma, \tag{29}$$

where the coefficients a_0–a_6 are

$$\zeta=(1-\mathrm{e}^{-2\xi})^{-2}/(1+A), \tag{30}$$

$$a_0=\frac{\zeta}{\left(1+A\mathrm{e}^{-2\xi}\right)\left(1+2A-3A\mathrm{e}^{-2\xi}\right)}, \tag{31}$$

$$a_1=2-9\mathrm{e}^{-2\xi}+15\mathrm{e}^{-4\xi}-8\mathrm{e}^{-6\xi}-6\mathrm{e}^{-8\xi}, \tag{32}$$

$$a_2=5-17\mathrm{e}^{-2\xi}+10\mathrm{e}^{-4\xi}+20\mathrm{e}^{-6\xi}, \tag{33}$$

$$a_3=2+5\mathrm{e}^{-2\xi}-25\mathrm{e}^{-4\xi}, \tag{34}$$

$$a_4=2-11\mathrm{e}^{-2\xi}+24\mathrm{e}^{-4\xi}-20\mathrm{e}^{-6\xi}-\mathrm{e}^{-8\xi}, \tag{35}$$

$$a_5=3-9\mathrm{e}^{-2\xi}-5\mathrm{e}^{-4\xi}+34\mathrm{e}^{-6\xi}-5\mathrm{e}^{-8\xi}, \tag{36}$$

$$a_6=1+5\mathrm{e}^{-2\xi}-22\mathrm{e}^{-4\xi}-2\mathrm{e}^{-6\xi}. \tag{37}$$

At the third-order $O(\epsilon^3)$, the solutions for $\eta^u_{3,3}$ and $\eta^l_{3,3}$ are derived as

$$\eta^u_{3,3} = \frac{k^2}{2}b_0\alpha_+\Xi^3\mathrm{e}^{-2\xi}(b_1A^6+b_2A^5+b_3A^4 +2b_4A^3-b_5A^2-b_6A+b_7)\cosh^3\Gamma, \tag{38}$$

$$\eta^l_{3,3} = \frac{k^2}{8}b_0\Xi^3(b_8A^6+2b_9A^5+b_{10}A^4 +2b_{11}A^3+b_{12}A^2-2b_{13}A+b_{14})\cosh^3\Gamma, \tag{39}$$

where the coefficients b_0–b_{14} are shown in Appendix A.

The third-order feedback to the fundamental mode solutions $\eta^u_{3,1}$ and $\eta^l_{3,1}$ is

$$\eta^u_{3,1} = -\frac{k^2}{16}c_0\alpha_+\Xi^3(c_1A^6+c_2A^5+c_3A^4 +2c_4A^3+c_5A^2-c_6A+c_7)\cosh^3\Gamma, \tag{40}$$

$$\eta^l_{3,1} = -\frac{k^2}{16}c_0\Xi^3(c_8A^6+c_9A^5+c_{10}A^4 +2c_{11}A^3+c_{12}A^2+c_{13}A+c_{14})\cosh^3\Gamma, \tag{41}$$

where the coefficients c_0–c_{14} are shown in Appendix A. To validate these analytical solutions, we employ the fourth-order Runge–Kutta method to numerically solve the coupled second-order ordinary differential equations. The analytical and numerical results will be presented and compared in the subsequent discussion. When $A=1$, the third-order WN solutions at the upper and lower interfaces reduce to

$$\begin{cases}\eta^u_1=\left[1-\frac{1}{4}k^2\left(\eta^u_{\mathrm{L}}\right)^2\left(1+\frac{3}{2}\mathrm{e}^{2\xi}\right)\right]\eta^u_{\mathrm{L}},\\ \eta^u_2=-\frac{1}{2}k\left(\eta^u_{\mathrm{L}}\right)^2,\\ \eta^u_3=\frac{3}{8}k^2\left(\eta^u_{\mathrm{L}}\right)^3,\end{cases} \tag{42}$$

$$\begin{cases}\eta^l_1=\left[1-\frac{1}{4}k^2\left(\eta^l_{\mathrm{L}}\right)^2\left(\frac{3}{2}+\mathrm{e}^{2\xi}\right)\right]\eta^l_{\mathrm{L}},\\ \eta^l_2=-\frac{1}{2}k\left(\eta^l_{\mathrm{L}}\right)^2,\\ \eta^l_3=\frac{3}{8}k^2\left(\eta^l_{\mathrm{L}}\right)^3,\end{cases} \tag{43}$$

where $\eta^l_{\mathrm{L}}=\Xi\cosh\tau$ and $\eta^u_{\mathrm{L}}=\Xi\,\mathrm{e}^{-\xi}\cosh\tau$ are the linear results at the upper and lower interfaces. The present analysis confirms that the reduced WN solutions in Eqs. (42) and (43) reproduce the typical solutions of Ref. [28] for a finite-thickness fluid layer.

3. Weakly nonlinear analysis

In this section, we investigate the WN perturbation growth at both the upper and lower interfaces. The linear growth rate of perturbations at the lower interface is discussed in Subsection 3.1. In Subsections 3.2–3.4, we systematically analyze three initiation scenarios: (1) RTI development from lower interface perturbations alone, (2) upper interface perturbations alone, and (3) simultaneous perturbations at both interfaces. The saturation amplitudes of the fundamental mode are subsequently investigated in Subsection 3.5.

To simulate WN evolution of the double interface, we employ an Eulerian-based fluid simulation code.[32] The hydrodynamic behavior is governed by the ideal gas equation of state, with a CFL number of 0.3 to ensure numerical stability. The computational domain in this study is configured as $L\times 5L$ (where $L=\lambda$, the characteristic wavelength), with a constant acceleration of 1000 cm/μs^2 applied along the vertical ($5L$) direction. The intermediate region between the two interfaces has a fixed density of 3.5 g/cm^3, while the upper region has a density of 0.001 g/cm^3. The lower region density can be adjusted in the simulations. Periodic boundary conditions are imposed in the x-direction to maintain consistent perturbation structures across the domain, whereas wall boundary conditions are applied in the y-direction. The numerical scheme utilizes a finite-volume approach with large-scale parallel computation for efficiency. A second-order HLLE approximate Riemann solver[33] is employed, complemented by a Moncen slope limiter[34] to enhance solution accuracy and numerical stability.

3.1. Linear growth rate

The linear growth rate of the perturbations at the lower interface is influenced by the Atwood number A and shell thickness ξ. Figure 2 illustrates the linear growth rate versus the Atwood number for shell thicknesses $\xi=0.1$, 0.3, 0.6, and 1.0. For $A=1$, the linear growth rate γ matches the Taylor form $\gamma_{\mathrm{c}}=\sqrt{kg}$, and the finite thickness of the shell in this case does not alter the linear growth rate for any values of ξ. For a finite density of the light fluid ($A\neq 1$), a smaller shell thickness ξ results in a reduced linear growth rate. In the limit of $\xi\gg 1$, the perturbations grow at the same rate as in the system of two semi-infinite fluids, given by $\gamma=\sqrt{Akg}$. As can be seen, the simulation results show excellent agreement with the linear growth rate.

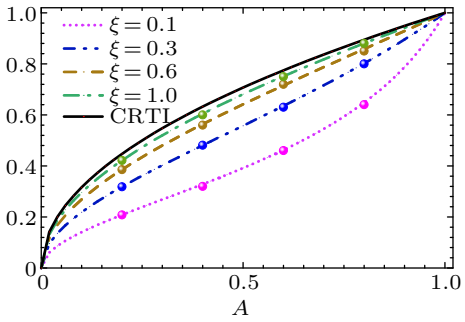


Fig. 2. Linear growth rate of the perturbations at lower interface versus Atwood number A for $\xi = 0.1$ (dotted), 0.3 (short-dashed), 0.6 (dashed), and 1.0 (dot-dashed). The growth rate of CRTI is included for comparison. The symbols represent corresponding numerical results.

3.2. Lower interface perturbations

We first investigate the WN growth of RTI initiated exclusively by a lower interface perturbation ($l_0 = 0.001\lambda$ and $u_0 = 0$) for a shell thickness $\xi = 0.6$. Figure 3 presents the temporal evolution of the normalized amplitudes for the first three perturbation harmonics (η_1/λ, $-\eta_2/\lambda$, and η_3/λ) on both upper and lower interfaces, considering different Atwood numbers $A = 1.0$, 0.8, and 0.6. The corresponding numerical results, denoted by symbolic markers in the figure, are compared across different Atwood number conditions.

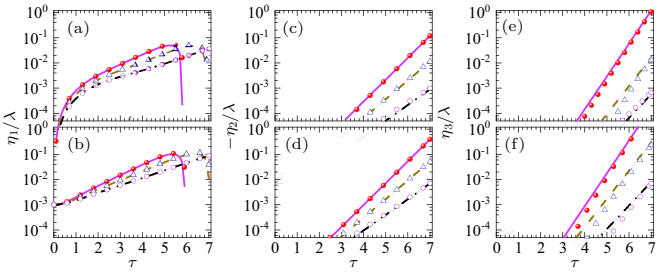


Fig. 3. Temporal evolution of normalized perturbation amplitudes for the fundamental mode [(a), (b)], second harmonic [(c), (d)] and third harmonic [(e), (f)] on the upper [(a), (c), (e)] and lower [(b), (d), (f)] interfaces initiated by only the lower interface perturbation with $A = 1.0$ (solid), 0.8 (dashed) and 0.6(dot-dashed), respectively. Symbol markers denote corresponding numerical results. The initial conditions are $l_0 = 0.001\lambda$ and $u_0 = 0$.

As can be seen, the fundamental perturbation modes on both interfaces exhibit exponential growth in the early phase ($0 < \tau < 4$). As amplitudes increase, the growth of the fundamental modes deviates from linear (exponential) behavior due to third-order negative feedback effects (nonlinear mode-coupling phenomena). This nonlinear suppression persists until a characteristic maximum amplitude threshold is reached. Beyond this critical point, the theoretical model predicts unphysical rapid amplitude decay, indicating that the present model's validity boundary lies below this maximum amplitude. As demonstrated in Fig. 3, under fixed time τ conditions, the normalized amplitudes of the first three perturbation harmonics exhibit a monotonic decrease with decreasing Atwood number. This means the density contrast plays a crucial role in modulating perturbation growth at both the upper and lower interfaces. The upper interface displays significantly smaller perturbation amplitudes compared to the lower interface. This phenomenon primarily arises from the dominant feedthrough mechanism, in which perturbation growth at the upper interface is principally driven by nonlinear interactions with perturbations at the lower interface.

Figure 4 illustrates the temporal evolution of the finite-thickness shell initialized only by the lower interface perturbation at $t = 0$, 2, and 3 ns. The WN results are shown in Figs. 4(a)–4(c), while Figs. 4(a′)–4(c′) present the corresponding numerical simulations. In the simulations, the shell thickness is set to $d = 15$ μm, and the lower region density is $\rho = 0.25$ g/cm^3. The lower interface perturbation is $l_0 = 0.01\lambda$ (where $\lambda = 40\pi$ μm). In this configuration, the upper interface is RT-stable and initially unperturbed, while the lower interface undergoes RTI. It can be observed that the initially stable upper interface becomes unstable, while significant perturbation growth occurs at both interfaces, as the RT growth at the lower interface rapidly feeds through to the upper interface, resulting in substantial deformation of the fluid layer. The analytical results are consistent with the numerical simulation results.

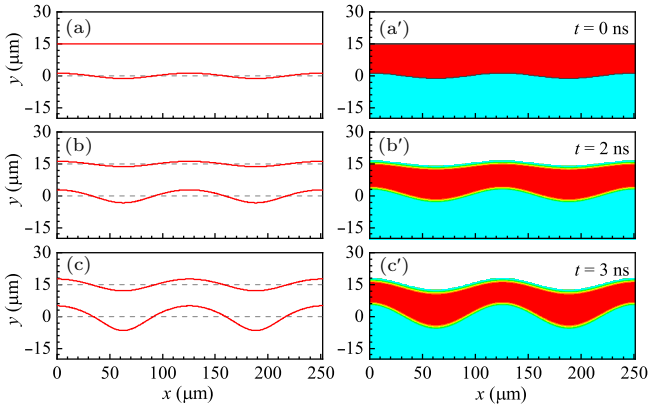


Fig. 4. Evolution of interface positions obtained by the present model [(a)–(c)], and numerical simulation [(a′)–(c′)] at the same time. The lower interface is initially perturbed with perturbation wavelength $\lambda = 40\pi$ μm.

3.3. Upper interface perturbations

When perturbations are imposed exclusively on the upper interface, namely, $u_0 = 0.005\lambda$ and $l_0 = 0$, the linear solutions are

$$\eta^u_{1,1} = \frac{1}{1-\alpha_+\alpha_-}u_0\left(\cos\tau - \alpha_+\alpha_-\cosh\Gamma\right), \tag{44}$$

$$\eta^l_{1,1} = \frac{\alpha_-}{1-\alpha_+\alpha_-}u_0\left(\cos\tau - \cosh\Gamma\right). \tag{45}$$

As can be seen from the analytical expressions, the perturbation phase at the lower interface exhibits a π-shift relative to the initial upper-interface perturbation. This phase-shift effect depends on the Atwood number at the interface. When the Atwood number $A < 0$, such as at the upper interface (a vacuum/fluid interface, where $A = -1$), a phase reversal occurs

compared to the initial perturbations at the upper interface. In contrast, when $A > 0$ at the lower interface, perturbations propagating to the upper interface maintain the same phase as those at the lower interface. Figure 5 explicitly illustrates this phase relationship through the temporal evolution of interface positions perturbed solely by upper-interface perturbations at $\xi = 0.2$ for normalized times $\tau = 0$, 0.38, 0.6, and 1.0. Initially, a perturbation is applied to the upper (initially stable) interface while the lower (RT-unstable) interface remains unperturbed. The perturbation amplitude at the upper interface first decreases with increasing τ, reaches zero at $\tau \approx 0.6$, and subsequently increases with a phase reversal. Conversely, the lower interface's perturbation amplitude grows monotonically with τ while maintaining a negative phase. This phenomenon originates from the inherent linear stability of the upper interface, manifesting as temporal oscillations that induce a predominant downward motion. Concurrently, phase inversion emerges during the propagation of perturbations. When the upper-interface perturbation propagates to the lower interface, the inherently linearly unstable interface triggers phase inversion. Following RTI initiation at the lower interface, the resulting perturbation feeds back to the upper interface. Ultimately, both interfaces synchronize to identical perturbation phases, as confirmed in Fig. 5.

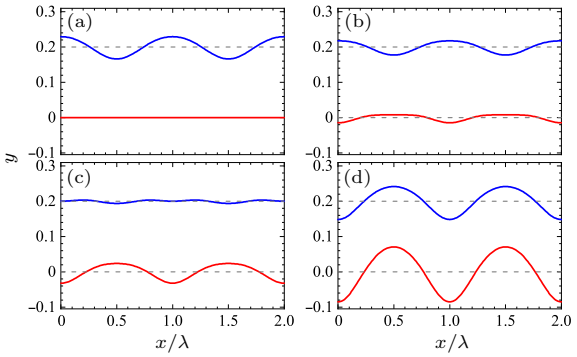


Fig. 5. Temporal evolution of the upper and lower interface positions initiated by only the upper interface perturbation for $\xi = 0.2$ at $\tau = 0$ (a), 0.38 (b), 0.6 (c), and 1.0 (d), respectively. The initial conditions are $u_0 = 0.005\lambda$ and $l_0 = 0$.

3.4. Both upper and lower interface perturbations

We investigate the RTI initiated by perturbations simultaneously imposed at both the upper and lower interfaces. The initial phases of perturbations on the two interfaces are allowed to be different. Specifically, the in-phase case for $l_0 = u_0 = 0.001\lambda$ and the out-of-phase case for $l_0 = -u_0 = 0.001\lambda$ are systematically discussed.

The temporal evolution of normalized amplitudes for the first three perturbation harmonics with $A = 1.0$, 0.8, and 0.6 at both upper and lower interfaces is demonstrated. In Fig. 6, both interfaces are initially perturbed with equal amplitudes of $l_0 = u_0 = 0.001\lambda$. For comparison, the corresponding out-of-phase case is presented in Fig. 7. As illustrated in Fig. 6, the perturbation growth of the first three perturbation harmonics is significantly slower in the in-phase case compared to the out-of-phase case demonstrated in Fig. 7. This phenomenon arises from a negative feedback mechanism: as perturbations at the upper interface propagate downward, their interaction with lower-interface perturbations diminishes the amplitude of perturbations at the lower interface, thereby suppressing harmonic growth in the in-phase case. The Atwood number plays a critical role in perturbation growth. Across both the in-phase and out-of-phase cases, a large Atwood number leads to significantly amplified perturbation growth at both upper and lower interfaces. Particularly in the out-of-phase configuration, the Atwood number demonstrates a more pronounced influence on upper interface perturbations.

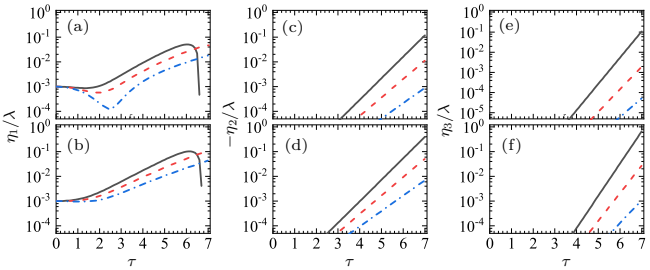


Fig. 6. Temporal evolution of normalized amplitudes of the fundamental mode [(a), (b)], second [(c), (d)] and third [(e), (f)] harmonics on the upper [(a), (c), (e)] and lower [(b), (d), (f)] interfaces initiated by both the upper and lower interface perturbations with $A = 1.0$ (solid), 0.8 (dashed) and 0.6 (dot-dashed) for $\xi = 0.6$, respectively. The initial conditions are $l_0 = u_0 = 0.001\lambda$.

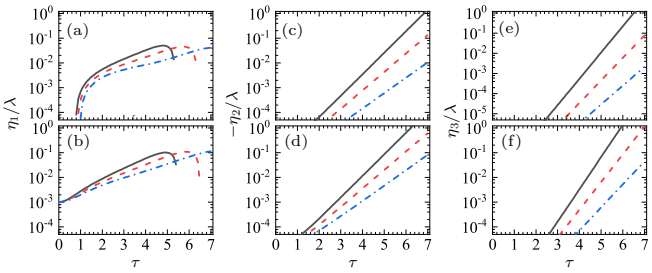


Fig. 7. Temporal evolution of normalized amplitudes of the fundamental mode [(a), (b)], second [(c), (d)] and third [(e), (f)] harmonics on the upper [(a), (c), (e)] and lower [(b), (d), (f)] interfaces initiated by both the upper and lower interface perturbations with $A = 1.0$ (solid), 0.8 (dashed), and 0.6 (dashed-dotted) for $\xi = 0.6$, respectively. The initial conditions are $l_0 = -u_0 = 0.001\lambda$.

The discrepancy in the positions of the lower interface between the present model and that from the classical single-interface case (CRTI)[12] for $A = 0.8$ is analyzed. As demonstrated in Figs. 8 (in-phase case) and 9 (out-of-phase case), significant discrepancies are observed between the lower interface positions predicted by our model and those calculated for the CRTI. Notably, the CRTI systematically overestimates perturbation growth for the in-phase case (Fig. 8), while significantly underestimating perturbation growth in the out-of-phase case (Fig. 9). The perturbation phase difference exhibits particular significance in ICF implosions, where both configurations may manifest. Crucially, our results demonstrate that

finite-thickness fluid layers subjected to out-of-phase perturbations exhibit a critical growth significantly exceeding predictions from two semi-infinite fluid models.

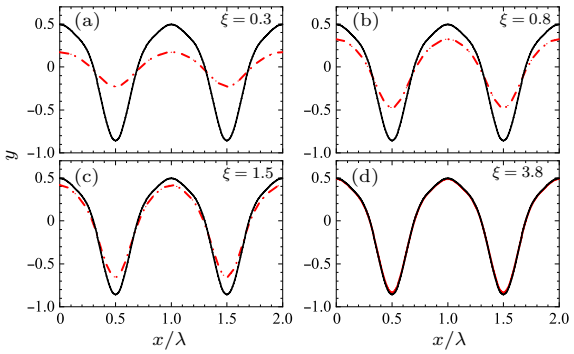


Fig. 8. Comparison of the position of the lower interface obtained from the present model (dashed) with that calculated by the CRTI (solid) initiated by both the upper and lower interface perturbations at $\tau = 6.0$ for $\xi = 0.3$ (a), 0.8 (b), 1.5 (c), and 3.8 (d), respectively. The initial conditions are identical to those in Fig. 6.

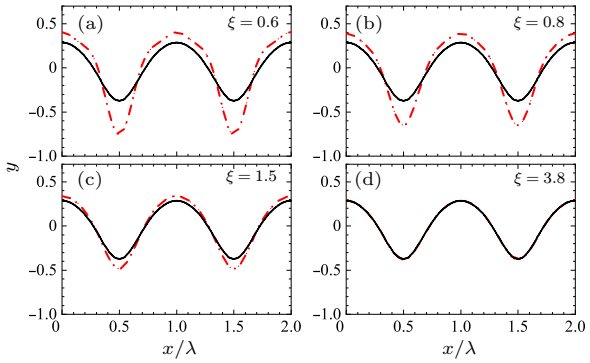


Fig. 9. Comparison of the position of the lower interface obtained from the present model (dashed) with that calculated by the CRTI (solid) initiated by both the upper and lower interface perturbations at $\tau = 5.2$ with $\xi = 0.6$ (a), 0.8 (b), 1.5 (c), and 3.8 (d), respectively. The initial conditions are identical to those in Fig. 7.

In order to investigate shell deformation, the temporal evolution of normalized shell thicknesses at the bubble vertex (d_{bubble}) and spike tip (d_{spike}) is analyzed. Figure 10 presents the temporal evolution of normalized layer thickness at these critical locations, initiated by both upper and lower interface perturbations across different Atwood numbers A. The results demonstrate that d_{spike} increases with time τ while d_{bubble} decreases with time τ, revealing significant deformation of finite-thickness fluid layers under RTI. Furthermore, the larger Atwood number leads to significantly enhanced perturbation growth in both bubbles and spikes, indicating increased shell thickness deformation driven by interface coupling effects. Compared with the in-phase case, the growth of bubbles and spikes is much more severe in the out-of-phase case. Therefore, special attention must be paid to cases where perturbations at the interfaces have a negative phase during ICF implosion.

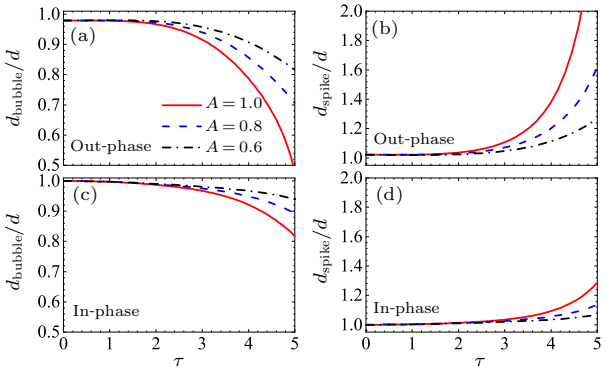


Fig. 10. Temporal evolution of the normalized layer thicknesses at the bubble vertex [(a), (c)] and the spike tip [(b), (d)] for $A = 1.0$ (solid), 0.8 (dashed), and 0.6 (dot-dashed), respectively. The initial conditions are $l_0 = -u_0 = 0.001\lambda$ for out-of-phase case [(a), (b)] and $l_0 = u_0 = 0.001\lambda$ for in-phase case [(c), (d)].

3.5. Nonlinear saturation amplitudes

The nonlinear saturation amplitudes (NSA) of the fundamental mode, incorporating corrections up to third order, are derived as follows. The NSA of the fundamental mode, denoted as η^i_{1s}, is defined as the linear growth amplitude at saturation time when the fundamental mode growth η^i_1 exhibits a 10% reduction relative to the linear growth η^i_L; specifically, when $(\eta^i_L - \eta^i_1)/\eta^i_L = 10\%$. Accordingly, the normalized NSAs of the fundamental mode for the upper (η^u_{1s}) and lower (η^l_{1s}) interfaces, incorporating third-order corrections, are expressed as

$$\frac{\eta^u_{1s}}{\lambda} = \frac{1}{\pi}\sqrt{\frac{2}{5c_0\left(A^6c_1 + A^5c_2 + A^4c_3 + 2A^3c_4 + A^2c_5 - Ac_6 + c_7\right)}}, \tag{46}$$

$$\frac{\eta^l_{1s}}{\lambda} = \frac{1}{\pi}\sqrt{\frac{2}{5c_0\left(A^6c_8 + A^5c_9 + A^4c_{10} + 2A^3c_{11} + A^2c_{12} + Ac_{13} + c_{14}\right)}}. \tag{47}$$

For the case of Atwood number $A = 1$, Eqs. (46) and (47) can be reduced to

$$\begin{cases} \dfrac{\eta^u_{1s}}{\lambda} = \dfrac{1}{\pi}\sqrt{\dfrac{1}{15+10\mathrm{e}^{-2\xi}}}, \\ \dfrac{\eta^l_{1s}}{\lambda} = \dfrac{1}{\pi}\sqrt{\dfrac{1}{10+15\mathrm{e}^{-2\xi}}}, \end{cases} \tag{48}$$

which is identical to the results of NSA for a finite-thickness slab. In the limit of $\xi \to \infty$, the classical NSA of $\sim 0.1\lambda$ is obtained.[10]

Figure 11 shows the dependence of NSA for the fundamental perturbation mode on the Atwood number A at the

upper and lower interfaces for different shell thicknesses. As shown in Fig. 11, when the thickness is $\xi > 0.5$, the NSA at the upper interface decreases rapidly with increasing Atwood number, while the NSA at the lower interface exhibits a gradual decrease. For $\xi < 0.5$, the NSA at the upper interface first decreases rapidly and then gradually increases with increasing Atwood number, whereas the NSA at the lower interface shows a slow monotonic increase with the Atwood number. For a fixed A, the NSA at both the upper and lower interfaces increases with increasing layer thickness ξ. For a thin-shell case with $\xi = 0.3$, the NSA exhibits a monotonic increase from $\sim 0.04\lambda$ to $\sim 0.074\lambda$ at the lower interface and from $\sim 0.045\lambda$ to $\sim 0.07\lambda$ at the upper interface as A increases. Specifically, in realistic ICF implosions, the NSA of the fundamental mode at unstable interfaces (including the ablator-fuel interface in acceleration, and the hot-spot boundary in deceleration) can be substantially below the classical 0.1λ prediction. It is noteworthy that a small NSA corresponds to an earlier onset of nonlinear growth of RTI. For ICF implosions, increasing the shell thickness or decreasing the interfacial Atwood number is an effective approach to enhance the saturation amplitude. It's found that ablation effects tend to increase the saturation amplitude of the RTI growth for a single-interface case,[13] particularly for short-wavelength perturbations.

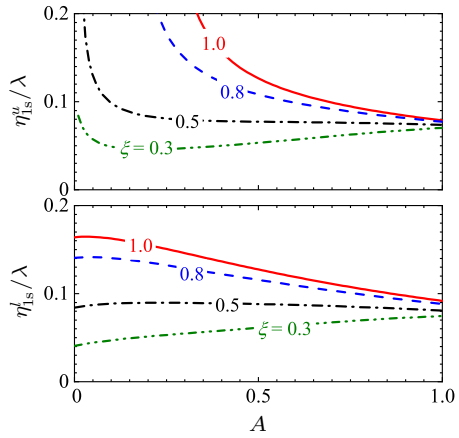


Fig. 11. The NSA η^i_{1s}/λ of the fundamental mode on the upper (a) and lower interfaces (b) versus the Atwood number A for different shell thicknesses ξ.

4. Conclusion

This paper presents a third-order WN theoretical framework to investigate single-mode RTI in a finite-thickness fluid layer supported by a semi-infinite fluid. The analytical results are in excellent agreement with the numerical simulation results. Our analysis demonstrates that the linear growth rate of perturbations at the lower interface is governed by both the Atwood number A and shell thickness ξ. Specifically, both smaller Atwood numbers and thinner shells (smaller ξ) lead to reduced perturbation growth rates. The derived coupling coefficients α_- and α_+ quantitatively describe how perturbations propagate between interfaces, revealing enhanced coupling effects for thin shells ($\xi < 1$). When perturbations from the initially stable interface feedthrough to the unstable interface, they exhibit a π-phase shift relative to the initial stable interface perturbations. The out-of-phase initial conditions lead to significantly faster growth than in-phase cases, suggesting phase control may be a potential instability mitigation strategy in ICF. The saturation amplitudes at both interfaces depend on ξ and A, showing significant deviations from classical predictions. Our model enables quantitative prediction of perturbation feedthrough between interfaces, incorporating fluid density ratio across the interface. Furthermore, it may provide valuable insights for identifying critical interfaces requiring special attention in ICF implosions. Additionally, this analytical model can serve as a verification benchmark for numerical simulation codes applied to RTI in ideal fluid layers.

Appendix A

The coefficients b_0–b_{14} for $\eta^u_{3,3}$ and $\eta^l_{3,3}$ are

$$b_0 = a_0\zeta/[\left(2+(1+A)\,\mathrm{e}^{-2\xi}+2A\,\mathrm{e}^{-4\xi}\right)\left(1+3A-4A\,\mathrm{e}^{-2\xi}\right)],$$
$$b_1 = 12-100\,\mathrm{e}^{-2\xi}+343\,\mathrm{e}^{-4\xi}-568\,\mathrm{e}^{-6\xi}+310\,\mathrm{e}^{-8\xi}+350\,\mathrm{e}^{-10\xi}-512\,\mathrm{e}^{-12\xi}+69\,\mathrm{e}^{-14\xi}+78\,\mathrm{e}^{-16\xi}+72\,\mathrm{e}^{-18\xi},$$
$$b_2 = 52-368\,\mathrm{e}^{-2\xi}+937\,\mathrm{e}^{-4\xi}-708\,\mathrm{e}^{-6\xi}-943\,\mathrm{e}^{-8\xi}+1718\,\mathrm{e}^{-10\xi}-274\,\mathrm{e}^{-12\xi}-372\,\mathrm{e}^{-14\xi}-366\,\mathrm{e}^{-16\xi},$$
$$b_3 = 67-301\,\mathrm{e}^{-2\xi}+78\,\mathrm{e}^{-4\xi}+1464\,\mathrm{e}^{-6\xi}-2036\,\mathrm{e}^{-8\xi}-561\,\mathrm{e}^{-10\xi}+1436\,\mathrm{e}^{-12\xi}+663\,\mathrm{e}^{-14\xi},$$
$$b_4 = 5+95\,\mathrm{e}^{-2\xi}-542\,\mathrm{e}^{-4\xi}+608\,\mathrm{e}^{-6\xi}+724\,\mathrm{e}^{-8\xi}-1069\,\mathrm{e}^{-10\xi}-361\,\mathrm{e}^{-12\xi},$$
$$b_5 = 44-323\,\mathrm{e}^{-2\xi}+337\,\mathrm{e}^{-4\xi}+1105\,\mathrm{e}^{-6\xi}-1414\,\mathrm{e}^{-8\xi}-559\,\mathrm{e}^{-10\xi},$$
$$b_6 = 32-22\,\mathrm{e}^{-2\xi}-375\,\mathrm{e}^{-4\xi}+424\,\mathrm{e}^{-6\xi}+265\,\mathrm{e}^{-8\xi},$$
$$b_7 = 7-54\,\mathrm{e}^{-2\xi}+48\,\mathrm{e}^{-4\xi}+53\,\mathrm{e}^{-6\xi},$$
$$b_8 = 48-436\,\mathrm{e}^{-2\xi}+1624\,\mathrm{e}^{-4\xi}-2857\,\mathrm{e}^{-6\xi}+1276\,\mathrm{e}^{-8\xi}+3668\,\mathrm{e}^{-10\xi}-6206\,\mathrm{e}^{-12\xi}+2949\,\mathrm{e}^{-14\xi}+222\,\mathrm{e}^{-16\xi}-72\,\mathrm{e}^{-18\xi},$$

$$b_9 = 68 - 466\mathrm{e}^{-2\xi} + 956\mathrm{e}^{-4\xi} + 513\mathrm{e}^{-6\xi} - 4457\mathrm{e}^{-8\xi} + 4618\mathrm{e}^{-10\xi} + 1726\mathrm{e}^{-12\xi} - 4221\mathrm{e}^{-14\xi} + 543\mathrm{e}^{-16\xi} + 72\mathrm{e}^{-18\xi},$$
$$b_{10} = 124 - 385\mathrm{e}^{-2\xi} - 1134\mathrm{e}^{-4\xi} + 5244\mathrm{e}^{-6\xi} - 1808\mathrm{e}^{-8\xi} - 12123\mathrm{e}^{-10\xi} + 10172\mathrm{e}^{-12\xi} + 5460\mathrm{e}^{-14\xi} - 2526\mathrm{e}^{-16\xi} + 216\mathrm{e}^{-18\xi},$$
$$b_{11} = 11 + 161\mathrm{e}^{-2\xi} - 716\mathrm{e}^{-4\xi} - 577\mathrm{e}^{-6\xi} + 4600\mathrm{e}^{-8\xi} - 2413\mathrm{e}^{-10\xi} - 4096\mathrm{e}^{-12\xi} + 837\mathrm{e}^{-14\xi} + 33\mathrm{e}^{-16\xi},$$
$$b_{12} = -26 + 248\mathrm{e}^{-2\xi} + 212\mathrm{e}^{-4\xi} - 2611\mathrm{e}^{-6\xi} + 880\mathrm{e}^{-8\xi} + 4240\mathrm{e}^{-10\xi} + 498\mathrm{e}^{-12\xi} - 201\mathrm{e}^{-14\xi},$$
$$b_{13} = 7 - 17\mathrm{e}^{-2\xi} - 120\mathrm{e}^{-4\xi} + 8\mathrm{e}^{-6\xi} + 503\mathrm{e}^{-8\xi} + 261\mathrm{e}^{-10\xi} + 6\mathrm{e}^{-12\xi},$$
$$b_{14} = -2 - 3\mathrm{e}^{-2\xi} + 18\mathrm{e}^{-4\xi} + 80\mathrm{e}^{-6\xi} + 84\mathrm{e}^{-8\xi} + 39\mathrm{e}^{-10\xi}.$$

The coefficients c_0–c_{14} for $\eta^u_{3,1}$ and $\eta^l_{3,1}$ are

$$c_0 = a_0\zeta(1-\mathrm{e}^{-2\xi})/[(1-A\mathrm{e}^{-2\xi})(1+9A-10A\mathrm{e}^{-2\xi})],$$
$$c_1 = 54 - 447\mathrm{e}^{-2\xi} + 1453\mathrm{e}^{-4\xi} - 2168\mathrm{e}^{-6\xi} + 870\mathrm{e}^{-8\xi} + 1382\mathrm{e}^{-10\xi} - 1226\mathrm{e}^{-12\xi} - 392\mathrm{e}^{-14\xi} + 480\mathrm{e}^{-16\xi},$$
$$c_2 = 213 - 1600\mathrm{e}^{-2\xi} + 4503\mathrm{e}^{-4\xi} - 5342\mathrm{e}^{-6\xi} + 1632\mathrm{e}^{-8\xi} + 428\mathrm{e}^{-10\xi} + 1418\mathrm{e}^{-12\xi} - 1288\mathrm{e}^{-14\xi},$$
$$c_3 = 309 - 1741\mathrm{e}^{-2\xi} + 2964\mathrm{e}^{-4\xi} - 410\mathrm{e}^{-6\xi} - 2634\mathrm{e}^{-8\xi} + 1008\mathrm{e}^{-10\xi} + 594\mathrm{e}^{-12\xi},$$
$$c_4 = 90 - 122\mathrm{e}^{-2\xi} - 1094\mathrm{e}^{-4\xi} + 3182\mathrm{e}^{-6\xi} - 2777\mathrm{e}^{-8\xi} + 694\mathrm{e}^{-10\xi} - 33\mathrm{e}^{-12\xi},$$
$$c_5 = 6 + 643\mathrm{e}^{-2\xi} - 2369\mathrm{e}^{-4\xi} + 2244\mathrm{e}^{-6\xi} - 308\mathrm{e}^{-8\xi} - 126\mathrm{e}^{-10\xi},$$
$$c_6 = 33 - 220\mathrm{e}^{-2\xi} + 195\mathrm{e}^{-4\xi} + 22\mathrm{e}^{-6\xi} + 6\mathrm{e}^{-8\xi},$$
$$c_7 = -9 + 49\mathrm{e}^{-2\xi} - 88\mathrm{e}^{-4\xi} + 54\mathrm{e}^{-6\xi},$$
$$c_8 = 54 - 375\mathrm{e}^{-2\xi} + 773\mathrm{e}^{-4\xi} + 550\mathrm{e}^{-6\xi} - 4924\mathrm{e}^{-8\xi} + 8124\mathrm{e}^{-10\xi} - 4968\mathrm{e}^{-12\xi} + 52\mathrm{e}^{-14\xi} + 720\mathrm{e}^{-16\xi},$$
$$c_9 = 141 - 752\mathrm{e}^{-2\xi} + 525\mathrm{e}^{-4\xi} + 3922\mathrm{e}^{-6\xi} - 8612\mathrm{e}^{-8\xi} + 3132\mathrm{e}^{-10\xi} + 4848\mathrm{e}^{-12\xi} - 3240\mathrm{e}^{-14\xi},$$
$$c_{10} = 141 - 387\mathrm{e}^{-2\xi} - 736\mathrm{e}^{-4\xi} + 1784\mathrm{e}^{-6\xi} + 3796\mathrm{e}^{-8\xi} - 8968\mathrm{e}^{-10\xi} + 4392\mathrm{e}^{-12\xi} + 68\mathrm{e}^{-14\xi},$$
$$c_{11} = 43 - 26\mathrm{e}^{-2\xi} - 103\mathrm{e}^{-4\xi} - 674\mathrm{e}^{-6\xi} + 1510\mathrm{e}^{-8\xi} - 714\mathrm{e}^{-10\xi} - 96\mathrm{e}^{-12\xi},$$
$$c_{12} = 44 - 77\mathrm{e}^{-2\xi} + 197\mathrm{e}^{-4\xi} - 534\mathrm{e}^{-6\xi} + 600\mathrm{e}^{-8\xi} - 140\mathrm{e}^{-10\xi},$$
$$c_{13} = 13 - 36\mathrm{e}^{-2\xi} + 161\mathrm{e}^{-4\xi} - 294\mathrm{e}^{-6\xi} + 120\mathrm{e}^{-8\xi},$$
$$c_{14} = 1 - \mathrm{e}^{-2\xi} + 6\mathrm{e}^{-4\xi}. \tag{A1}$$

Acknowledgements

Project supported by the Fundamental Research Funds for the Central Universities (Grant No. 2025ZKPYNY05), the National Science and Technology Major Project of China (Grant No. 2024ZD1700201), and the Strategic Priority Research Program of Chinese Academy of Sciences (Grant Nos. XDA 25051000 and XDA 25010100).

References

[1] Rayleigh L 1882 *Proc. London Math. Soc.* **s1-14** 170
[2] Taylor G 1950 *Proc. R. Soc. Lond. A* **201** 192
[3] Inogamov N A 1999 *Anstrophys. Space Phys.* **1** 10
[4] Betti R and Hurricane O A 2016 *Nat. Phys.* **12** 435
[5] Wang L F, Ye W H, He X T, *et al*. 2017 *Sci. China Phys. Mech. Astron.* **60** 055201
[6] Zylstra A B, Hurricane O A, Callahan D A, *et al*. 2022 *Nature* **601** 542
[7] Clark D S, Weber C R, Milovich J L, *et al*. 2019 *Phys. Plasmas* **26** 050601
[8] Guo Y, Wu D and Zhang J 2024 *Phys. Plasmas* **31** 112106
[9] Li J, Yan R, Zhao B, *et al*. 2024 *Phys. Plasmas* **31** 012703
[10] Liu W H, Wang L F, Ye W H, *et al*. 2012 *Phys. Plasmas* **19** 042705
[11] Lai H L, Xu A G, Zhang G C, *et al*. 2016 *Phys. Rev. E* **94** 023106
[12] Wang L F, Ye W H, He X T, *et al*. 2012 *Phys. Plasmas* **19** 100701
[13] Wang L F, Ye W H and He X T 2012 *Phys. Plasmas* **19** 012706
[14] Xin J, Yan R, Wan Z H, *et al*. 2019 *Phys. Plasmas* **26** 032703
[15] Zhang D, Li J, Xin J, *et al*. 2022 *Phys. Plasmas* **29** 072702
[16] Mikaelian K O 1982 *Phys. Rev. A* **26** 2140
[17] Mikaelian K O 1983 *Phys. Rev. A* **28** 1637
[18] Mikaelian K O 2025 *Phys. Fluids* **37** 032114
[19] Guo H Y, Wang L F, Ye W H, *et al*. 2017 *Chin. Phys. Lett.* **34** 075201
[20] Guo H Y, Wang L F, Ye W H, *et al*. 2017 *Chin. Phys. B* **26** 125202
[21] Guo H Y, Wang L F, Ye W H, *et al*. 2018 *Chin. Phys. B* **27** 025206
[22] Li Z Y, Wang L F, Wu J F, *et al*. 2020 *Chin. Phys. Lett.* **37** 025201
[23] Huang L X, Xiao D L, Wang X G, *et al*. 2025 *Phys. Plasmas* **32** 052714
[24] Wilkinson J P and Jacobs J W 2007 *Phys. Fluids* **19** 124102
[25] Ding J C, Si T, Yang J M, *et al*. 2017 *Phys. Rev. Lett.* **119** 014501
[26] Raman K S, Smalyuk V A, Casey D T, *et al*. 2014 *Phys. Plasmas* **21** 072710
[27] Hurricane O A, Callahan D A, Casey D T, *et al*. 2014 *Phys. Plasmas* **21** 056314
[28] Wang L F, Guo H Y, Wu J F, *et al*. 2014 *Phys. Plasmas* **21** 122710
[29] Guo H Y, Wang L F, Ye W H, *et al*. 2017 *Phys. Plasmas* **24** 112708
[30] Guo H Y, Cheng T, Li J and Li Y J 2022 *Chin. Phys. B* **31** 035203
[31] Miller S C and Goncharov V N 2022 *Phys. Plasmas* **29** 082701
[32] Li Z Y, Wang L F, Wu J F, *et al*. 2020 *Acta Mech. Sin.* **36** 789
[33] Einfeldt B 1988 *SIAM Journal on Numerical Analysis* **25** 294
[34] Roe P L 1986 *Ann. Rev. Fluid Mech.* **18** 337